

Swin-X2S: Reconstructing 3D Shape from 2D Biplanar X-ray with Swin Transformers

Kuan Liu*, Zongyuan Ying*, Jie Jin*, Dongyan Li*, Ping Huang*, Wenjian Wu*, Zhe Chen*, Jin Qi*, Yong Lu[†], Lianfu Deng*, and Bo Chen*

Abstract

The conversion from 2D X-ray to 3D shape holds significant potential for improving diagnostic efficiency and safety. However, existing reconstruction methods often rely on hand-crafted features, manual intervention, and prior knowledge, resulting in unstable shape errors and additional processing costs. In this paper, we introduce Swin-X2S, an end-to-end deep learning method for directly reconstructing 3D segmentation and labeling from 2D biplanar orthogonal X-ray images. Swin-X2S employs an encoder-decoder architecture: the encoder leverages 2D Swin Transformer for X-ray information extraction, while the decoder employs 3D convolution with cross-attention to integrate structural features from orthogonal views. A dimension-expanding module is introduced to bridge the encoder and decoder, ensuring a smooth conversion from 2D pixels to 3D voxels. We evaluate proposed method through extensive qualitative and quantitative experiments across nine publicly available datasets covering four anatomies (femur, hip, spine, and rib), with a total of 54 categories. Significant improvements over previous methods have been observed not only in the segmentation and labeling metrics but also in the clinically relevant parameters that are of primary concern in practical applications, which demonstrates the promise of Swin-X2S to provide an effective option for anatomical shape reconstruction in clinical scenarios. Code implementation is available at: <https://github.com/liukuan5625/Swin-X2S>.

1. Introduction

X-ray imaging is an essential tool for preliminary clinical assessments and is widely used in emergency care, or-

*Department of Orthopaedics, Shanghai Key Laboratory for Prevention and Treatment of Bone and Joint Diseases, Shanghai Institute of Traumatology and Orthopaedics, Ruijin Hospital, Shanghai Jiao Tong University School of Medicine, Shanghai 200025, China.

[†]Department of Radiology, Ruijin Hospital Luwan Branch, School of Medicine, Shanghai Jiaotong University, Shanghai 200003, China.

thopedics, dentistry, and routine health check-ups due to its cost-effectiveness, low radiation exposure, and rapid imaging capabilities. However, its inherent 2D structure limits its ability to distinguish spatial shapes and intricate anatomical details. In contrast, CT scans offer high-resolution 3D representations, providing comprehensive views of bones, organs, blood vessels, and soft tissues, making them ideal for detecting subtle abnormalities. But CT scans are significantly more costly, entail higher radiation exposure, and require longer processing time.

The challenge of reconstructing 3D shape from 2D X-ray images has attracted long-lasting attention due to its potential capability to provide the interest anatomical structures for preliminary diagnosis and treatment in an economical, safe, and rapid manner [1, 2, 3, 4, 5]. Especially in poverty-stricken areas where access to CT scanners is limited or unavailable [6, 7], and for underdeveloped children who must undergo CT radiation exposure, such as those with scoliosis or fractures [8, 9], the importance of 2D-3D reconstruction becomes even more pronounced to these vulnerable populations.

Early approaches to 3D shape reconstruction relied on hand-crafted features, including point-based, contour-based, statistical shape model (SSM) based, and active shape model (ASM) based algorithms. These methods require manual intervention and prior knowledge of anatomical geometry, leading to unacceptable shape error and processing time in clinical practice. With the development of deep learning, there has been a shift toward data-driven methods that automatically learn patterns from data. These approaches, such as convolution neural networks (CNNs) [10, 11] and Transformers [12], have shown promise in overcoming the limitations of traditional methods [13]. Deep neural networks are capable of directly reconstructing 3D structures from X-ray images, thereby reducing the reliance on physician expertise and improving both accuracy and efficiency. Nevertheless, the effectiveness of deep learning algorithms heavily depends on the quality and diversity of annotated datasets, and existing methods typically design distinct algorithms for different anatomies, some of

which require specific data processing methods [4, 5].

In this paper, we propose a novel end-to-end deep learning-based method called Swin-X2S for directly reconstructing 3D segmentation and labeling from biplanar raw X-ray images. The proposed algorithm employs a 2D transformer-based encoder and a 3D convolution-based decoder, with a dimension-expanding module to bridge 2D pixels and 3D voxels. To evaluate the performance of proposed method, we conduct thorough experiments across 9 publicly available datasets, covering 54 osseous structures from four anatomical regions (femur, hip, spine, and rib). We report segmentation and labeling results, along with shape errors in clinically relevant parameters.

2. Related work

Reconstructing 3D structures from 2D projections is an inverse problem that is inherently ill-posed and computationally challenging. Moreover, the arbitrary field of view (FOV), the distortion of X-ray projection, the presence of related diseases and metal implants introduce further challenges. To address above problems, existing studies resort to non-learning methods align with prior knowledge and data-driven deep learning approaches.

Traditional methods rely on a combination of anatomical prior knowledge, geometric landmarks and statistical features. Early works identified spatial landmarks of each vertebra from biplanar X-rays to determine the configuration of vertebral column [1, 14, 15]. In order to reduce human intervention and reconstruction time, semi-automated statistical methods [16, 2, 17, 18, 19, 20] have been proposed that utilize hand-crafted features (points, contours, atlases or deformation fields) to construct SSMs or ASMs for reconstructing various anatomical regions (vertebrae, hips, femurs, wrists). Despite incorporating statistical inferences, these methods still require manual pre-processing or post-processing steps to handle complex morphologies, which introduce extra human error and processing cost.

As deep learning methods have gained wider adoption in medical image processing, researchers have proposed data-driven algorithms to reduce user supervision. Some of these methods aim to develop neural networks incorporate with traditional method to improve feature extraction and model efficiency [8, 21, 22]. For example, Aubert et al. [8] utilized CNNs to develop a realistic SSM of spine from biplanar X-ray images for automatic vertebral column reconstruction; Oral-3D [22] reconstructed 3D structure of oral cavity based on prior information of the dental arch from a single panoramic X-ray.

At the same time, scholars also have proposed purely deep learning algorithms that eliminate the reliance on hand-crafted features and instead learn shape distributions directly from the training data. Some approaches first reconstruct raw CT images from X-ray projections and

then perform 3D segmentation on the reconstructed CT [4, 23, 24, 25]. For instance, X2CT-GAN [4] was the first method proposed to reconstruct raw CT images from two orthogonal X-ray images in an end-to-end manner. Shen et al. [23] introduced a deep learning framework to generate volumetric tomography from a single X-ray image. X-CTRSNet [24] and PerX2CT [25] both adopt encoder-decoder architecture to further enhance the reconstruction performance. However, reconstructed raw CT usually suffers from blurry volumes and missing details, which introduces difficulties in subsequent segmentation tasks.

Methods that directly reconstruct 3D shape from X-rays have demonstrated superior performance simultaneously. Kasten et al. [26] presented an end-to-end CNN approach for 3D shape reconstruction of knee bones directly from biplanar X-ray images. Several other studies [27, 28, 29, 30] have demonstrated the feasibility of algorithms for reconstructing anatomical structures such as the wrist, pelvis, vertebrae, and liver from corresponding X-ray images. For anatomical structures with strong similarities, such as vertebrae or ribs, different parts of overall morphology often appear highly alike, making them challenging to differentiate in X-ray images even for experienced radiologists. Most existing methods employ additional processes to address this challenge [30, 31, 32, 5]. BX2S-Net [31] is able to segment each vertebra of spine with high accuracy, however, their method requires known spatial location of each vertebra to crop raw image into patches, each containing individual vertebra images, before performing shape reconstruction. Wu et al.[32] proposed a spine localization and identification method from multi-view projection images, which localizes the centroid of each vertebra but does not establish its shape, with labeling serves as a necessary condition for segmentation.

These aforementioned methods generally require customized network designs and dataset processing pipelines tailored to specific structures, which limits their applicability. A recent study [5] introduced a benchmark of 3D bone shape reconstruction from biplanar X-ray images, performing four anatomies (femur, hip, spine and rib) 3D shape reconstruction across 6 public datasets. This work shares a similar objective with our study, yet it only segments binary shape masks, and notably, their method also necessitates precise localization of each vertebra to crop raw X-ray images, which serves as a prerequisite for spine reconstruction. To the best of our knowledge, our proposed framework is the first capable of accommodating these four anatomical structures and producing 3D segmentation and labeling directly from biplanar 2D X-ray images.

3. Method

The particularity of 2D-3D reconstruction task lies in the mismatch dimensions of the input and output. As depicted

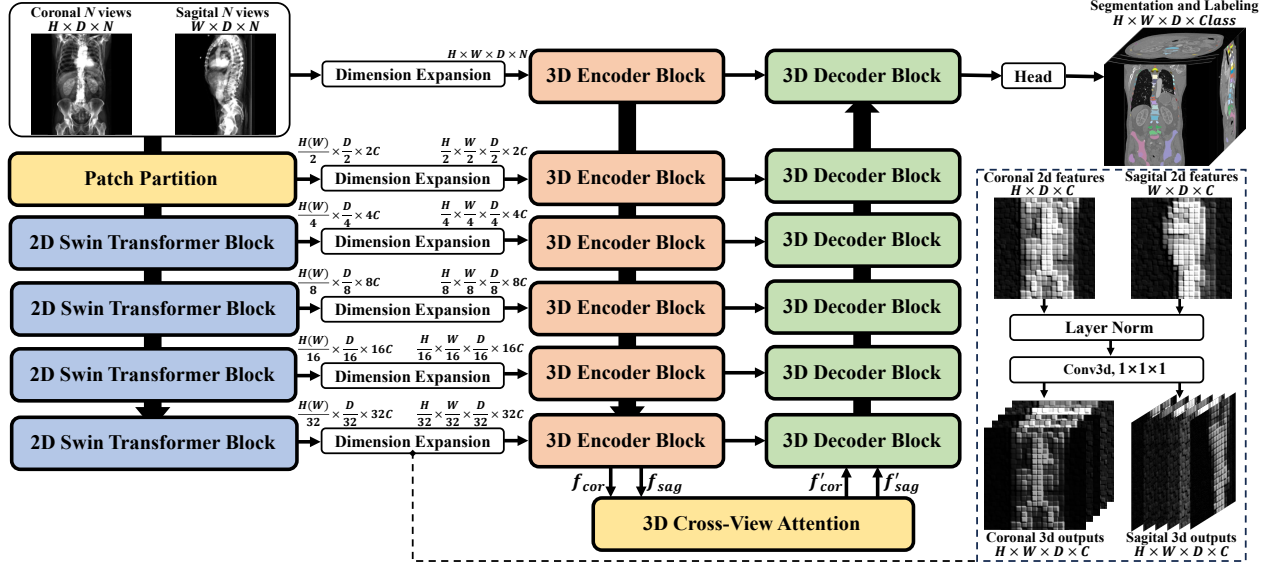


Figure 1. The overall architecture of the proposed Swin-X2S network for CT Segmentation and labeling from biplanar X-ray images ($N=1$). Swin-X2S takes paired inputs: the coronal view and sagittal view X-ray images. The network generates 2D pyramid features via transformers, which are applied to dimension expansion modules (right dashed box) for upscaling and then reconstruct through 3D U-shaped convolution network.

in Fig. 1, the overall architecture of Swin-X2S can be divided into three steps: (i) 2D Swin-Transformer-based encoder takes paired raw X-ray images as input to facilitate image feature extraction; (ii) Dimension-expanding module shuttles low-level tokens from 2D encoder to 3D decoder; (iii) 3D convolution-based decoder incorporates a cross-attention mechanism to fully integrate information from biplanar views, thereby enabling the shape reconstruction of various anatomies.

3.1. 2D Swin Transformer encoder

The inputs of Swin-X2S are $\chi_{cor} \in \mathbb{R}^{H \times D \times N}$ and $\chi_{sag} \in \mathbb{R}^{W \times D \times N}$, where $(H \times W \times D)$ represents the original CT scan size and N denotes the number of X-ray images (see section 4.1, $N=1$ denotes biplanar X-ray inputs). Embedded tokens are fed into successive Swin Transformer blocks [33] to generate 2D pyramid features. At block l , 2D tokens are divided into N non-overlapping $M \times M$ patches, each window patch conducts self-attention computation to establish pixel correlation. In the subsequent block $l+1$, 2D images are shifted by $(\frac{M}{2}, \frac{M}{2})$ pixels and then similarly divided into flattened windows to compute self-attention. Consecutive Swin Transformer blocks switch back and forth between patch windows and shifted patch windows. Specifically, the calculation is as follows:

$$\hat{z}^l = \text{W-MSA}(\text{LN}(z^{l-1})) + z^{l-1} \quad (1)$$

$$z^l = \text{MLP}(\text{LN}(\hat{z}^l)) + \hat{z}^l \quad (2)$$

$$\hat{z}^{l+1} = \text{W-MSA}(\text{LN}(z^l)) + z^l \quad (3)$$

$$z^{l+1} = \text{MLP}(\text{LN}(\hat{z}^{l+1})) + \hat{z}^{l+1} \quad (4)$$

W-MSA and SW-MSA are multi-head self-attention modules that alternate consecutively. The self-attention mechanism is formulated as:

$$\text{ATTN}(Q, K, V) = \text{softmax}\left(\frac{QK^T}{\sqrt{d}} + B\right)V \quad (5)$$

Where $Q, K, V \in \mathbb{R}^{H \times D \times N}$ denote queries, keys, and values respectively; B represents the relative position of tokens within each window.

3.2. Dimension expanding module

The dimension transformation issue does not arise in pure 2D or 3D encoder-decoder networks, however, the mapping from 2D images to 3D structures is essential in shape reconstruction task. It's evident that coronal photograph lack structural information from the sagittal view, and vice versa. We propose a simple and effective dimension expanding module, as illustrated in Fig. 1, to convert 2D pixel features to 3D voxel features at each output of 2D Swin Transformer patch merging stage. To be more specific, the coronal image and sagittal image are stacked into the same resolution of $\mathbb{R}^{H \times W \times D \times C}$ using $1 \times 1 \times 1$ 3D convolution kernels along sagittal and coronal axes, respectively. This alignment ensures that orthogonal 2D representations can be extracted and processed uniformly across different resolutions, enabling the integration of coherent and comprehensive information.

3.3. 3D U-shaped decoder

3D Decoder adopt U-shaped network design [34, 35, 36]. The contracted path processes high-dimensional tokens at each stage with dimensions of $(\frac{H}{2^i}, \frac{W}{2^i}, \frac{D}{2^i})$ where $i = 0, 1, 2, 3, 4, 5$, hierarchically compressing the relevant essential features. The expansive path takes the outputs from the previous stage and concatenates them with the opposite side via skip connections, progressively upsamples and refines latent tokens to original resolution. The final segmentation masks are reconstructed by the classification head.

At the bottleneck of the U-shaped network ($i = 5$), the cross-attention module is employed to integrate the high-level representations from different views. The fusion enables paired coronal view and sagittal view complement from each other to get spatial features which may be obstructed in original perspective. The cross-attention mechanism is formulated as follows:

$$CrossATTN(Q_i, K_j, V_j) = \text{softmax} \left(\frac{Q_i K_j^T}{\sqrt{d}} \right) V_j \quad (6)$$

In the equation, i and j represent different views, while Q_i , K_j , and V_j correspond to the query, key, and value matrices, respectively.

3.4. Model architecture

2D Swin Transformer is designed with four stages. A patch merging layer with a size of 2×2 is applied at the end of each stage to merge neighboring pixels. The 2D patch window size is set to 7×7 and the expansion ratio of MLP is set to $\alpha = 4$. 3D Decoder block consists of two successive $3 \times 3 \times 3$ convolution layers with residual connection, scaling up the channel and scaling down resolution by a factor of 2 during feature extraction, and operating the opposite way during feature aggregation. We introduced four types of our model: Swin-X2S-Tiny, Swin-X2S-Small, Swin-X2S-Base, and Swin-X2S-Large. The embedding dimension is set to 32, 64, 96, 128 respectively. The input size, output size, model size, theoretical computational complexity (FLOPs), and throughput of the model variants for CT scan are listed in Table 1. The model sizes of Swin-X2S-Tiny, Swin-X2S-Small, Swin-X2S-Large are approximately 0.1x, 0.5x, and 2x that of Swin-X2S-Base, respectively.

3.5. Loss function

The overall loss function of Swin-X2S consists two parts: one measures the similarity between single view predictions and ground truth, the other computes the difference between predictions from different view:

$$\mathcal{L}(p_i, q_i, y_i) = \frac{1}{2} (\mathcal{L}_{single}(p_i, y_i) + \mathcal{L}_{cross}(p_i, q_i) + \mathcal{L}_{single}(q_i, y_i) + \mathcal{L}_{cross}(q_i, p_i)) \quad (7)$$

where p , q and y represent the coronal predicted mask, sagittal predicted mask and ground truth label, respectively.

For single view loss part, we adopt DiceCE loss [37], which combines Dice Loss [38] and Cross Entropy Loss [39] to measure segmentation performance in a supervised manner; For cross view loss part, we adopt KL divergence loss [40] to quantify the difference between view in an unsupervised manner.

$$\mathcal{L}_{single} = 1 - \frac{1}{N} \sum_{i=1}^N \left(\frac{2|p_i \cap y_i|}{|p_i| + |y_i|} + y_i \log(p_i) \right) \quad (8)$$

$$\mathcal{L}_{cross} = \sum_{i=1}^N p_i \log \frac{p_i}{q_i} \quad (9)$$

while i denotes the i -th voxel of the total of N CT voxels.

4. Experimental setup

4.1. DRR generation

To evaluate our proposed method, a large dataset with paired biplanar images, corresponding CT slices, and segmentation masks is required. Furthermore, precise spatial alignment between CT and corresponding X-ray images is essential for accurate 3D reconstruction.

Due to the lack of such a dataset, most existing methods have applied digitally reconstructed radiograph (DRR) technique [41], a ray casting approach in which virtual rays are projected through 3D volumetric data to synthesize 2D radiographic images that mimicking conventional X-ray. Similarly, we use DRR technology to generate coronal and sagittal view groups by rotating ray source, producing N different view images at intervals of $90/N$ degrees from CT coronal and sagittal plane respectively, as shown in Fig. 2. Specifically, $N=1$ corresponds to orthogonal biplanar X-ray images. Based on the aforementioned methods, the original

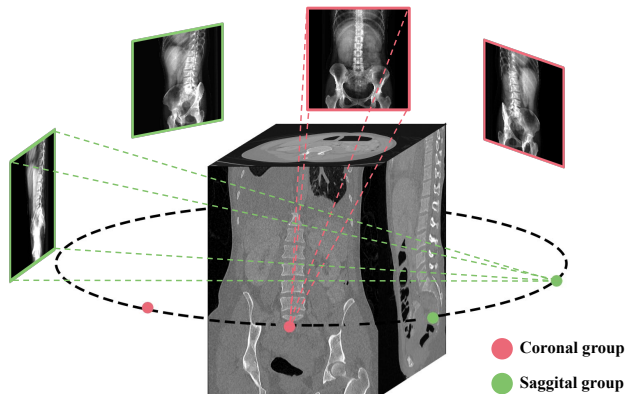


Figure 2. An example of generated coronal group and sagittal group based on DRR method, where the number of projection views N is set to 2.

Table 1. The model hyperparameters of the Swin-X2S network, "Hidden dimension" denotes the channel number of the hidden layers.

Model Architecture	Image Size	Hidden dimension	Block numbers	Head numbers	Parameters(M)	FLOPs(T)
Swin-X2S-Tiny	[96,96,128]	32	[2,2,6,2]	[1,2,4,8]	32.51	0.42
Swin-X2S-Small	[128,128,160]	64	[2,2,6,2]	[2,4,8,16]	129.97	3.35
Swin-X2S-Base	[128,128,160]	96	[2,2,18,2]	[3,6,12,24]	313.68	7.54
Swin-X2S-Large	[128,128,160]	128	[2,2,18,2]	[4,8,16,32]	557.58	13.38

dataset used for 3D medical image segmentation has been restructured into a new dataset consisting of paired X-ray scans and CT masks for reconstructing 3D shapes from 2D images.

4.2. Dataset

We have collected five large-scale public CT segmentation datasets to comprehensively evaluate the performance of our algorithm: (i) **Totalsegmentator**¹ [42] consists of 1228 CT scans and comprehensive labeling for multiple anatomical structures. (ii) **CTPelvic1K**² [33] comprises 1184 CT volumes, each with annotated sacrum, left hip, and right hip masks. (iii) **CTSpine1K**³ [43] contains 1005 CT volumes with labeled vertebrae masks. (iv) **VerSe'19** (Vertebral Segmentation Challenge 2019)⁴ [44] comprises 160 spinal CT scans with ground truth annotations. (v) **RibSeg v2**⁵ [45] contains 660 CT scans with binary rib annotations. These datasets were further subdivided into 9 subsets based on different anatomical structures, all of these subsets, with each subset following the official data split settings:

TotalSegmentator-Femur-Dataset 571 CT scans with femur masks were selected from the original TotalSegmentator dataset. This subset necessitates the segmentation of both the left and right femur.

TotalSegmentator-Pelvic-Dataset 1086 CT scans with pelvis masks were selected from the original TotalSegmentator dataset. This subset necessitates the segmentation of sacrum, left pelvis and right pelvis.

CTPelvic1K-Pelvic-Dataset CTPelvic1K consists of 1106 pelvis CT scans, this dataset necessitates the segmentation of 3 categories.

TotalSegmentator-Spine-Dataset 1189 CT scans with spine masks were selected from the original TotalSegmentator dataset. Angiography and overcropped scans were removed due to lack of context information. This subset necessitates the segmentation of 25 vertebrae categories.

CTSpine1K-Spine-Dataset CTSpine1K consists of 1005 spine CT scans, this dataset requires the segmentation of 25 categories.

¹<https://github.com/StanfordMIMI/TotalSegmentatorV2>

²<https://github.com/MIRACLE-Center/CTPelvic1K>

³<https://github.com/MIRACLE-Center/CTSpine1K>

⁴<https://github.com/anjany/verse>

⁵<https://github.com/M3DV/RibSeg>

VerSe'19-Spine-Dataset VerSe'19 consists of 160 spine CT scans, this dataset necessitates the segmentation of 25 classes.

TotalSegmentator-Rib-Dataset 1086 CT scans with rib masks were selected from the original TotalSegmentator dataset. Samples with angiocardiology or containing too few ribs were excluded. This subset necessitates the segmentation of twelve pairs of ribs, totaling 24 categories.

RibSeg v2-Rib-Dataset RibSeg v2 contains 660 CT scans, with most cases are confirmed with complete rib cages. Binary rib masks are re-assigned into 24 rib classes based on region connectivity.

TotalSegmentator-All-Dataset This dataset is the union of all the previous TotalSegmentator subsets, totaling 1005 CT scans, necessitates the segmentation of 4 anatomies comprising 54 categories.

4.3. Evaluation metrics

4.3.1 Segmentation and labeling metrics

We adopt segmentation and labeling metrics to evaluate the performance of reconstruction [44]. Segmentation metrics: (i) Dice Coefficient (Dice), a voxel overlap-based metric measures the quality of the segmentation which ranges from 0% (zero overlap) to 100% (perfect overlap). (ii) Hausdorff Surface Distance 95 (HD), distance-based metric measures the local maximum distance between the surface of prediction mask and the surface of ground truth; Labeling metrics: (i) Localization error (L-Error), a distance-based metric measures the average Euclidean distance between the ground truth centroids and the predicted segmentation centroids. (ii) Identification rate (ID-rate), accuracy-based metric measures the proportion of correctly identified instances out of the total number of target instances.

4.3.2 Clinically Relevant Metrics

For practical applications of 3D reconstruction, depending on the downstream task, clinical experts are more interested in the specific morphological structures of certain anatomical regions rather than overly general statistical segmentation or labeling metrics [46, 5]. Error assessment of morphological parameters for specific anatomies is a crucial step toward the practical application of 2D-3D reconstruction. We adopt automated clinical parameters evaluation pipelines to comprehensively analyze each sample: **Femur**

Table 2. Quantitative evaluation results of the 9 subsets using our proposed Swin-X2S-Base network with biplanar inputs. Dice score (Dice) and Hausdorff surface distance (HD) for segmentation evaluation, localization error (L-Error) and identification rate (ID-rate) for labeling evaluation.

Dataset	Segmentation results		Labeling results	
	Dice(%) \uparrow	HD(mm) \downarrow	L-error(mm) \downarrow	ID-rate(%) \uparrow
TotalSeg-Femur	92.31	4.79	2.79	99.07
TotalSeg-Pelvic	86.47	5.24	3.03	98.21
CTPelvic1K-Pelvic	89.11	4.66	2.57	98.79
TotalSeg-Spine	75.21	6.76	3.39	90.57
CTSpine1K-Spine	83.84	5.27	2.79	87.76
VerSe'19-Spine	64.54	10.77	7.43	77.23
TotalSeg-Rib	45.92	16.41	13.27	78.36
RibSeg v2-Rib	56.43	13.42	11.20	83.32
TotalSeg-All	57.51	13.33	9.22	83.56

Morphometry We adopt the method from [47] to measure Femoral Head Radius (FHR) and Neck Shaft Angle (NSA) from femur segmentation. **Pelvic Landmarks** Fischer et al. [48] automatically recognizes bony landmarks of the pelvis. We measure the landmark distance between prediction and ground truth. **Vertebra Morphometry** Di Angelo and Di Stefano [49] proposed an automatic method to identify geometric references and the associated dimensions. We employ this method to measure the morphological features of each vertebra in the reconstructed spine. **Rib Centerline** Jin et al. [45] emphasized the clinical importance of rib centerline. Following their pipeline, we automatically perform rib centerline extraction and evaluation.

4.4. Implementation details

Due to the arbitrary field of view (FOV) in CT scans, which exhibit varying orientations, resolutions, spacings, and scanning modes, all samples were projected to synthesis biplanar X-ray images based on DRR generation method. Paired coronal and sagittal X-rays were resized to 128×160 pixels with equal spacing on each axis, ground truth CT segmentation were correspondingly resampled to isotropic $128 \times 128 \times 160$ voxels to ensure strict alignment with projections. Data augmentation strategies including random zoom, rotation, shift, and flipping were applied. Our algorithm was implemented with PyTorch and MONAI framework and trained on Nvidia Tesla A100 GPU with 40GB memory. Pre-trained Swin Transformer networks on ImageNet-22K was employed as Swin-X2S encoder backbone. The network batch size was set to 1 and the initial learning rate is set as $3e-5$ with $5e-1$ weight decay. We trained our model with the AdamW [50] optimizer for 250 epochs, incorporating with warm-up cosine scheduler for the first 20 epochs.

5. Result and analysis

5.1. Result on different datasets

As shown in Table 2, we evaluated the reconstruction performance across 9 subsets using Swin-X2S-Base network, the labeling results were directly derived from the segmentation masks. Despite the data patterns exhibiting diverse orientations, resolutions, spacings, and scanning modes, Swin-X2S demonstrates robust reconstruction performance on different structures, as illustrated in Fig. 3. It is noteworthy that the task of spine and rib reconstruction is particularly challenging due to their high structural similarities. Among the three subsets for spine segmentation and labeling, Swin-X2S achieved a mean Dice of 83.84% on the CTSpine1K dataset, a mean Dice of 75.21% on the Totalsegmentator-Spine dataset and a slightly lower mean Dice of 64.54% for VerSe'19 dataset. The notable drop on the VerSe'19 dataset can be attributed to its relatively small data size, additionally, some samples were excessively cropped led to the absence contextual information, which in turn resulted the difficulties on vertebra identification (Fig. 4). Due to the inherently slender structure of ribs making them even harder to localize, proposed model achieves the lowest Dice of 45.92% and 56.43% on Rib-Seg v2 and Totalsegmentator-Rib dataset among all four anatomies. Most samples of Totalsegmentator-Rib exhibit modality diversity which resulting in incomplete rib cages and posing additional challenges for identification.

Moreover, we directly reconstruct all above four anatomies in the Totalsegmentator-All dataset. Proposed method achieves a mean Dice of 57.51% and mean HD 13.33 mm for segmentation, a mean L-error of 9.22 mm and mean ID-rate 83.56% for labeling. Overall, the performance of modeling all anatomies together is slightly lower than modeling each structure separately (Fig. 6).

5.2. Result on different methods

As shown in Table 3, we evaluated the reconstruction performance of several existing methods on CTPelvic1K, CTSpine1K, and Totalsegmentator-All dataset. The comparison methods adhered to the settings outlined in [5]. Notably, the regression head used for generating binary maps was replaced with classification head for segmentation and labeling.

Across these three tasks, Swin-X2S models achieve the state of art reconstruction performance. Previous deep learning methods suffer from the challenge of category confusion and fuzzy boundaries, where adjacent structures are not precisely separated by two boundary interfaces, as shown in Fig. 5, leading to segmentation inconsistencies inside anatomy. Transformer-based architecture, such as SwinUNETR [35] and AttentionUNet [54] generally performed better than pure CNN-based architecture. This superiority

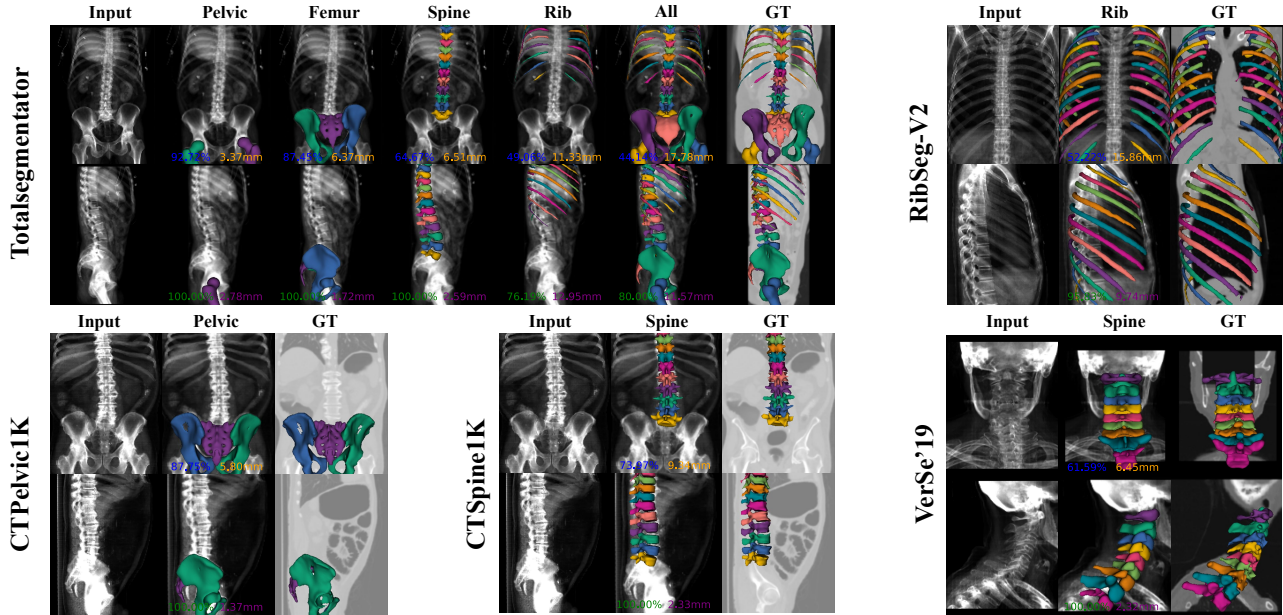


Figure 3. Quantitative reconstruction results of proposed Swin-X2S-Base network with biplanar inputs. Top-left panel: results of Totalsegmentator five subsets (femur, pelvis, spine, rib and all) on a single test sample. The first and second rows respectively exhibit the coronal and sagittal view. The first and last column denote biplanar inputs and ground truth, the other columns illustrate the segmentation results for different anatomies. The blue, orange, green and purple numbers respectively represent Dice, HD, L-error and ID-rate. Top-right panel: result of RibSeg v2 dataset on a single test sample. Bottom-left panel: result of CTPelvic1K. Bottom-center panel: result of CTSpine1K. Bottom-right panel: result of VerSe’19.

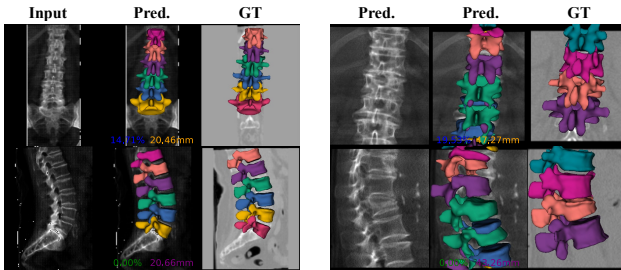


Figure 4. Reconstruction failure samples of Swin-X2S network on VerSe’19. The first, middle and last column denote biplanar inputs, prediction results and ground truth respectively

can be attributed to self-attention mechanism which captures global context effectively, while convolution mechanism inherently focuses on local spatial features. Feature-fusion methods like 2DConcat [29], UNet [53] and Mutiscale2DConcat [4] performed better than embedding vector fusion methods like 1DConcat [52] and TL-Embedding [51]. Fig. 5 visualizes comparison results between the ground truth segmentation and the shape reconstruction achieved by different networks. It can be seen that even for shifted, rotated, scaled and deformed structures, our method is able to segment category boundaries clearly, achieve the best reconstruction results among all algorithms.

Moreover, we present quantitative results of Swin-X2S

models with various architectural settings across these datasets. Swin-X2S-Tiny achieved the lowest mean Dice across these three reconstruction tasks. In comparison, Swin-X2S-Base performs slightly better than Swin-X2S-Small, with more substantial performance improvements observed for more difficult tasks. Despite the model size of Swin-X2S-Large is twice that of Swin-X2S-Base, its performance has barely improved. These experiments demonstrate the success of Swin-X2S owes not only to the larger number of parameters but also to the appropriate architecture settings.

5.3. Result on clinical metrics

Although automated shape feature extraction pipelines are robust at large, they still encounter additional errors introduced by mesh distortion and inaccurate localization. We evaluate the clinical metrics on Totalsegmentator-All as shown in Fig. 6. The quality of clinical shape estimation is generally positively correlated with the average Dice, however, there are exceptions such as (i) proposed Swin-X2S achieves the highest Dice on all four anatomies but performing worse than SwinUNETR in pelvic landmark especially for posterior superior iliac spine (PSIS); (ii) TL-Embedding and 1DConcat possess similar mean Dice, TL-Embedding completely fails in rib cage reconstruction, while 1DConcat performs much better in evaluating clinical parameters and

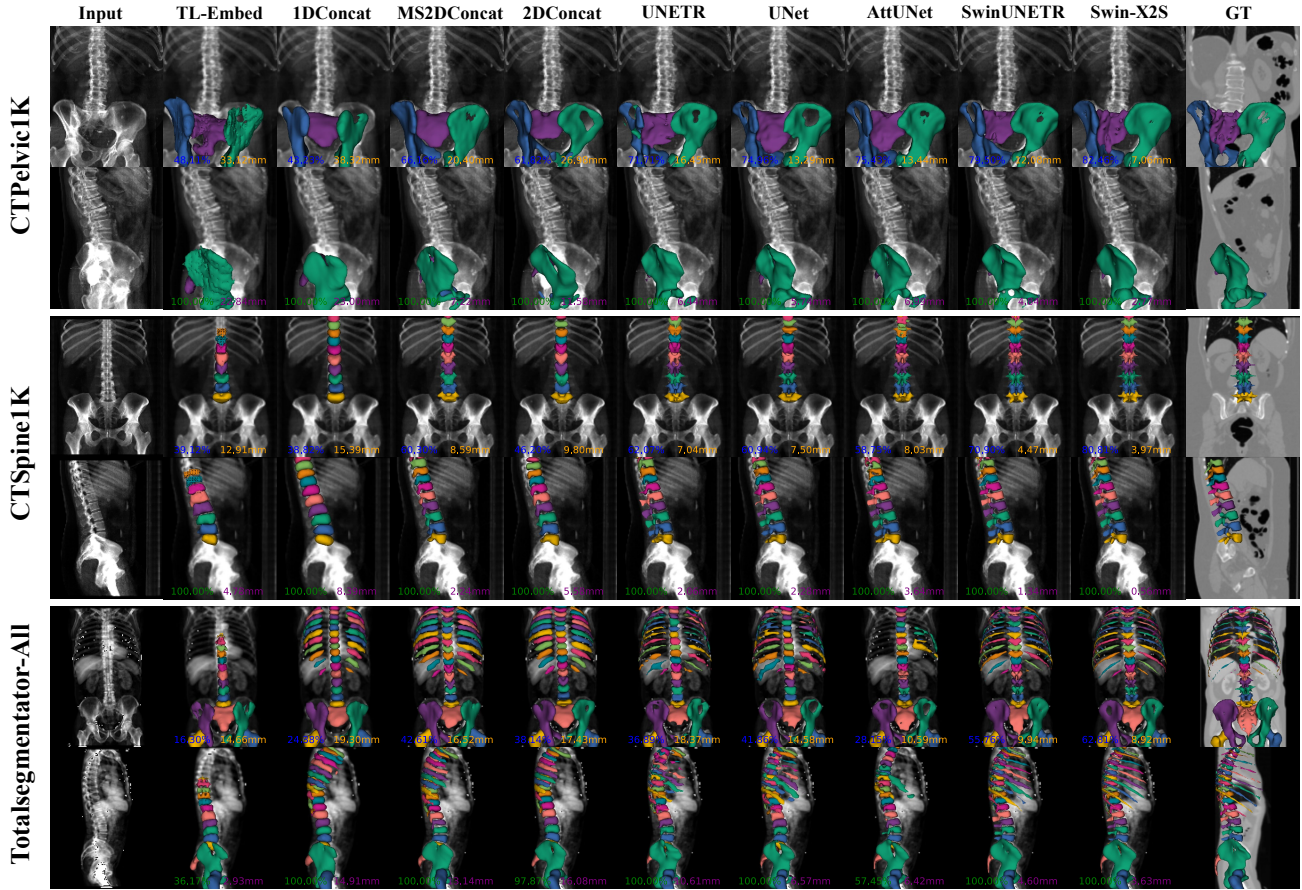


Figure 5. Comparison results of different methods on the CTPelvic1K, CTSpine1K, Totalsegmentator-All datasets with biplanar inputs. The first and the last columns of each dataset denote biplanar inputs and ground truth, the other columns illustrate prediction results of different methods.

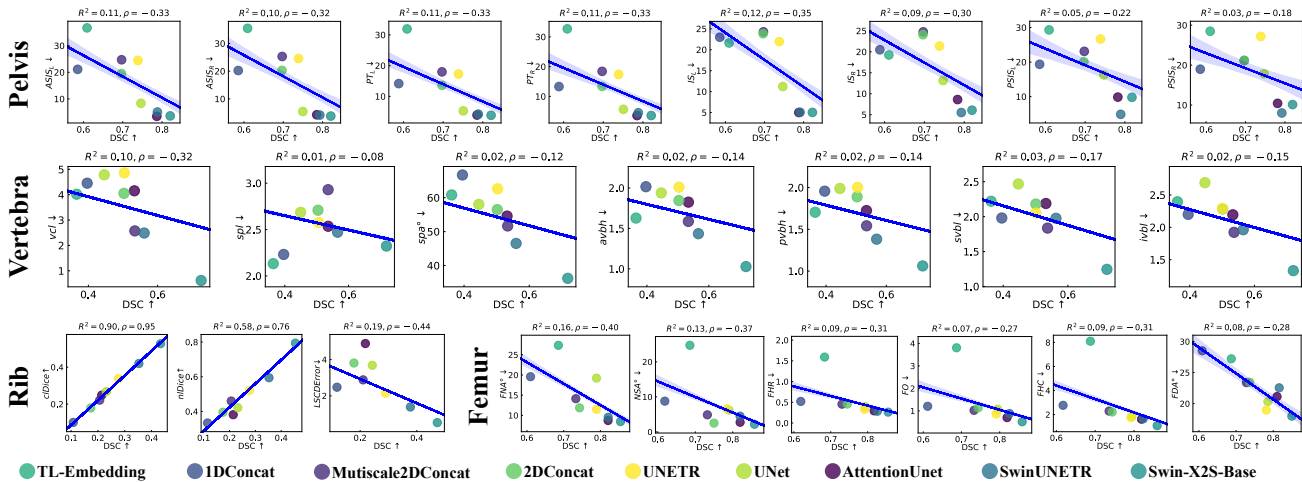


Figure 6. The correlation between the average Dice coefficient (x-axis) and clinical metrics (y-axis) on the Totalsegmentator-All dataset. The line denotes linear regression with confidence intervals of all reconstructed samples, and the scatter points represent the average value of corresponding algorithm's reconstructed samples.

Table 3. Comparison results of different models on the CTPelvic1K, CTSpine1K and Totalsegmentator-All datasets using biplanar inputs. The **bolded** numbers denote the highest score and the *italicized* numbers indicate the second highest.

Model (reference)	CTPelvic1K-dataset				CTSpine1K-dataset				Totalsegmentator-All-dataset			
	Dice(%)	HD(mm)	L-error(mm)	ID-rate(%)	Dice(%)	HD(mm)	L-error(mm)	ID-rate(%)	Dice(%)	HD(mm)	L-error(mm)	ID-rate(%)
TL-Embedding [51]	69.02	28.84	8.92	95.63	44.33	17.51	11.10	82.15	18.56	23.31	-	69.98
1DConcat [52]	69.57	20.39	9.75	93.51	53.64	17.38	10.45	81.51	27.41	41.51	25.23	53.65
Mutiscale2DConcat [4]	81.06	8.92	1.78	98.79	72.74	10.40	5.00	81.94	39.14	34.69	20.82	60.27
2DConcat [29]	80.77	9.51	5.02	98.79	63.35	12.88	6.69	92.34	35.72	64.79	23.72	57.93
UNETR [53]	83.42	9.41	4.44	99.10	63.51	16.53	8.56	71.99	37.84	37.18	20.78	58.79
UNet [26]	84.26	7.88	3.94	98.79	69.15	11.77	5.39	73.94	42.19	21.07	14.44	73.35
AttentionUnet [54]	84.90	7.45	3.84	98.64	69.53	10.36	5.21	81.47	33.08	19.03	10.15	82.84
SwinUNETR [35]	87.75	5.83	2.95	98.94	77.13	8.47	4.10	79.26	48.66	19.57	13.15	73.16
Swin-X2S-Tiny	83.20	5.31	2.95	98.52	74.44	8.47	5.10	82.58	44.81	22.46	15.31	79.57
Swin-X2S-Small	88.72	4.52	2.78	97.21	80.38	6.44	3.69	85.67	52.87	16.81	12.58	82.11
Swin-X2S-Base	<i>89.11</i>	<i>4.66</i>	2.57	<i>98.79</i>	83.84	5.27	2.79	84.76	<i>57.51</i>	<i>13.33</i>	9.22	83.56
Swin-X2S-Large	89.20	4.41	<i>2.60</i>	99.21	<i>83.41</i>	<i>5.44</i>	2.97	<i>85.18</i>	57.83	12.84	9.10	82.97

almost achieving results comparable to 2DConcat on pelvis and femur morphometry.

Swin-X2S achieves the best femoral head radius (FHR) and neck shaft angle (NSA) evaluation, which are crucial for the diagnosis of hip deformities and guidance of surgical planning for hip replacement. Pelvic landmarks, which are muscle and ligament attachment points, serve as key references for imaging diagnosis. SwinUNETR and AttentionUnet achieve similar Anterior Superior Iliac Spine (ASIS) localization compare to proposed method, even performs better on posterior ilium region. The correlation between vertebra parameters and Dice is the lowest, this is because we reconstruct the whole spine and then divide it into individual vertebrae, resulting in pixelated shape that introduces further challenges for evaluation. Nevertheless, Swin-X2S still shows significant improvements in determining the pedicle of vertebral arch area (vertebral canal length, vcl), which is the safe zone for pedicle screw insertion in spinal surgery. Although the average Dice of the ribs is the lowest among all structures, we observed that Swin-X2S achieved over 80% in nIDice, indicating that the main factor affecting shape accuracy is the axial deviation of centerline (LSCDError) rather than the curvature deviation of morphology (nIDice). The latter is a more valuable indicator for fracture detection and spinal deformities.

Table 4. Ablation study on the influence of the number of DRR views N on CTSpine1K dataset using Swin-X2S-Base network.

Num of views	Dice(%) \uparrow	HD(mm) \downarrow	L-error(mm) \downarrow	ID-rate(%) \uparrow
$N = 1$	83.84	5.27	2.79	87.76
$N = 2$	83.23	5.28	2.97	87.19
$N = 4$	83.99	5.20	2.89	87.67
$N = 10$	84.04	<i>5.05</i>	3.08	87.58
$N = 20$	<i>83.81</i>	4.95	3.00	87.33

5.4. Ablation study

5.4.1 The number of DRR views

We investigated the impact of the number of DRR views on performance in Table 4. As the number of projected views increases, there is a slight improvement (less than 1% improvement on Dice) in segmentation and annotation performance. This improvement can be attributed to the additional contextual information provided by the multi-view projections, which help to supplement occluded areas. However, non-coronal or non-sagittal images are unable aligned with ground truth masks, which may explain the limited marginal performance enhancement. Furthermore, more views come at the cost of proportional radiation dose and scanning time. Therefore, biplanar inputs are preferred for 2D-3D reconstruction task.

5.4.2 The effectiveness of key components

We perform ablation study to access the impact of key components of Swin-X2S on CTSpine1K using biplanar inputs (Table 5). First, we examined the effect of skip connections, the absence of transformer skip connections resulted in a significantly performance drop, with the mean Dice drop from 83.84% to 61.79%. The absence of convolution skip connections caused severe issues, leading to an untrainable model due to mode collapse. Unsupervised cross loss also plays an important role in training process, sole reliance on supervised loss lead to a noticeable mean Dice drop of 5.76%. Additionally, pre-trained Swin Transformer weights on ImageNet-22K facilitate network’s ability to learn generalized feature representations, resulting in improved reconstruction performance and faster convergence during training process, the base model experienced a drop 4.44% of mean Dice without pre-trained weights. Data augmentation strategies are crucial for generalization ability, particularly

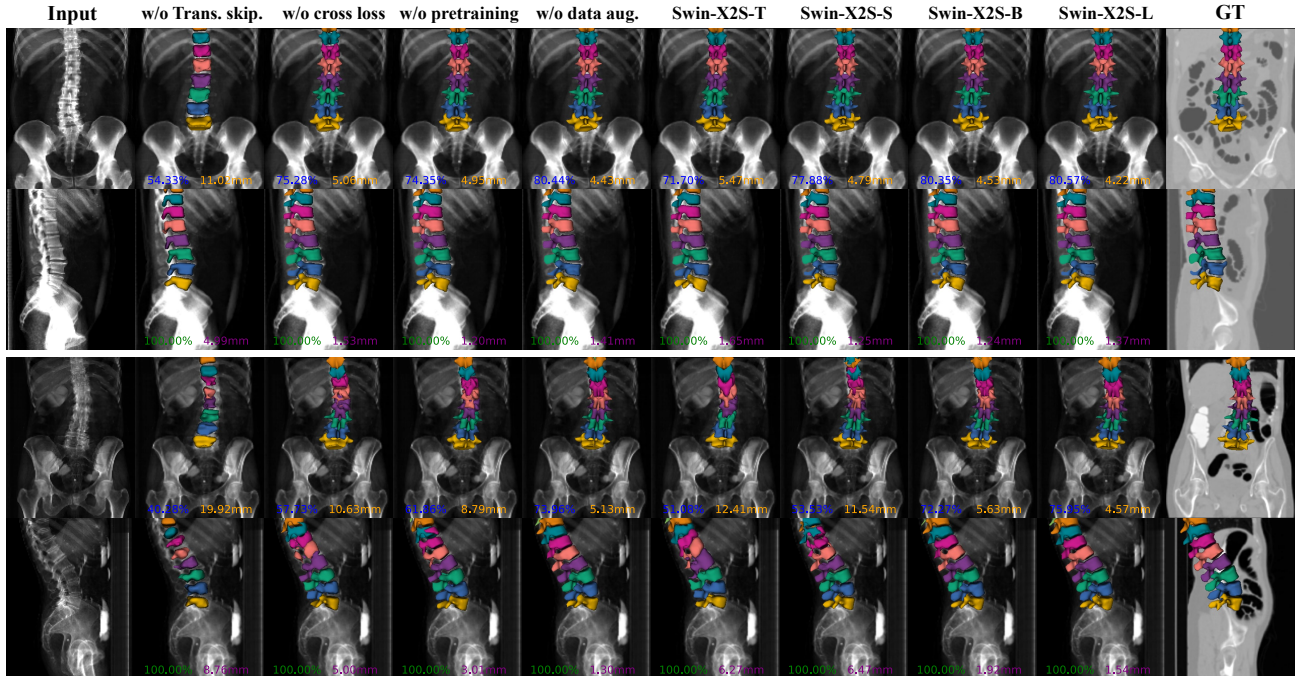


Figure 7. Ablation study of the key components of Swin-X2S on the CTSpine1K dataset with biplanar DRR inputs. Visualization results do not include the untrainable Swin-X2S-Base model without convolution skip connections.

for conditions like scoliosis, fracture and mental implants. The absence of this strategy lead to a decrease of 1.04% in segmentation (Dice) and an increase of 0.28 mm in labeling (L-error).

Table 5. Ablation study on the effect of model key components on CTSpine1K dataset using biplanar inputs. Trans. and conv. skip. mean transformer and convolution skip connection.

Model architecture	Dice(%)	L-error(mm)
Swin-X2S-Base w/o Trans. skip.	61.79	8.49
Swin-X2S-Base w/o conv. skip.	-	-
Swin-X2S-Base w/o cross loss	78.08	4.12
Swin-X2S-Base w/o pre-training	79.30	3.29
Swin-X2S-Base w/o data aug.	82.80	3.07
Swin-X2S-Tiny	74.44	5.10
Swin-X2S-Small	80.88	3.66
Swin-X2S-Base	83.84	2.79
Swin-X2S-Large	83.41	2.97

6. Discussion

We introduced a novel end to end method for the reconstruction of 3D bone shapes based on 2D X-ray images. Thoroughly experiments were evaluated across nine publicly available datasets covering four categories of skeleton anatomies. Experimental results showed that our method achieved the state of art reconstruction performance in both segmentation and labeling tasks. In terms of clinical

metrics, Swin-X2S demonstrates overall satisfactory performance, however, we observed that shape features are influenced by relatively unstable morphometry extraction pipelines, highlighting the need for further development of robust clinical parameter estimation methods to ensure effective evaluation in real-world scenarios.

DRR generation serves as a compromise solution due to the lack of datasets consisting of paired real X-ray images and aligned CT scans. The collection of such a dataset becomes an urgent task for reconstruction method research, requiring attention and effort. A collaborative effort from the community could help make these datasets more accessible to the public.

2D-3D reconstruction not only can be applied in preliminary diagnosis and treatment, it also holds potential for real-time 3D visualization in orthopedic surgeries assisted by mobile C-arm digital radiography in the future. Furthermore, our current work focuses solely on bone shape reconstruction, which could also be used to quickly locate and reshape foreign objects, such as metal implants or fragments. Exploring the reconstruction methods for non-osseous anatomical structures may also hold significant value of research.

Appendix

Appendix A. Comparison Network Architecture

All seven comparison model architectures were illustrated in table 6, the image resolution is set to [128, 128, 160] except for TL-Embedding and 1DConcat due to architecture constraint, the batch size was set to 1 for SwinUNETR and UNETR, 4 for MultiScale2DConcat and 8 for others, the initial learning rate is set as 2e-3 for UNETR and SwinUNETR and 2e-4 for the other models. For each dataset, the classification head was configured to corresponding class number, all architectures were trained with the AdamW optimizer for 50 epochs, with a warm-up cosine scheduler for the first 5 epochs.

Table 6. The model hyperparameters of the comparison methods.

Model Architecture	Image Size	Parameters(M)	FLOPs(G)
TL-Embedding	[128,128,128]	53.65	4.38
1DConcat	[128,128,128]	40.67	256.08
Multiscale2DConcat	[128,128,160]	3.08	365.55
2DConcat	[128,128,160]	1.55	1737.96
UNETR	[128,128,160]	95.77	499.92
UNet	[128,128,160]	1.31	569.06
AttentionNet	[128,128,160]	1.48	96.06
SwinUNETR	[128,128,160]	61.99	1978.90

Appendix B. Visualization of Feature Maps

As shown in fig. 8, we present the visualization results of feature maps in the Swin-X2S-Base skip connections trained on Totalsegmentator-All dataset. Swin-X2S consists of six stages, with each subsequent stage having half the resolution and twice the number of channels of the previous stage. The rows perspective exhibits that the deeper features possess the more compressed and abstract forms of expression, the columns perspective shows 2D Swin Transformer extract the basic features of X-rays, while 3D encoder and decoder focus on the segmentation and labeling of interest anatomies.

References

- [1] Richard H Brown, Albert H Burstein, Clyde L Nash, and Charles C Schock. Spinal analysis using a three-dimensional radiographic technique. *Journal of biomechanics*, 9(6):355–IN1, 1976.
- [2] Gabor T Herman. *Fundamentals of computerized tomography: image reconstruction from projections*. Springer Science & Business Media, 2009.

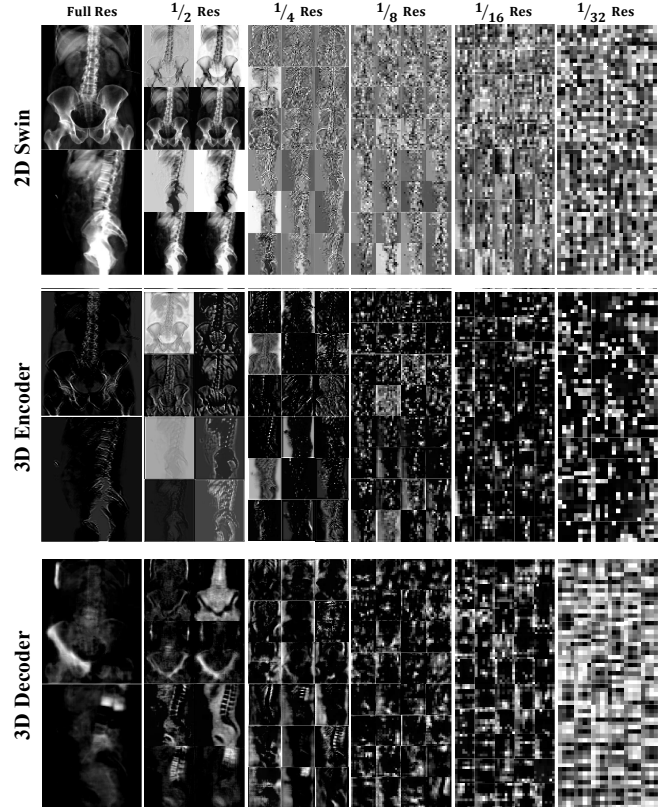


Figure 8. Visualization results of feature maps in Swin-X2S-Base skip connections. The first row, the middle row, and the last row denote the output of 2D Swin Transformer, 3D encoder, and 3D decoder at each stage, respectively.

- [3] S Hosseinian and H Arefi. 3d reconstruction from multi-view medical x-ray images—review and evaluation of existing methods. *The international archives of the photogrammetry, remote sensing and spatial information sciences*, 40:319–326, 2015.
- [4] Xingde Ying, Heng Guo, Kai Ma, Jian Wu, Zhengxin Weng, and Yefeng Zheng. X2ct-gan: reconstructing ct from biplanar x-rays with generative adversarial networks. In *Proceedings of the IEEE/CVF conference on computer vision and pattern recognition*, pages 10619–10628, 2019.
- [5] Mahesh Shakya and Bishesh Khanal. Benchmarking encoder-decoder architectures for biplanar x-ray to 3d bone shape reconstruction. *Advances in Neural Information Processing Systems*, 36, 2024.
- [6] Hedvig Hricak, May Abdel-Wahab, Rifat Atun, Miriam Mikhail Lette, Diana Paez, James A Brink, Lluís Donoso-Bach, Guy Frija, Monika Hierath, Ola Holmberg, et al. Medical imaging and nuclear

- medicine: a lancet oncology commission. *The Lancet Oncology*, 22(4):e136–e172, 2021.
- [7] Patrick Sitati Ngoya, Wilbroad Edward Muhogora, and Richard Denys Pitcher. Defining the diagnostic divide: an analysis of registered radiological equipment resources in a low-income african country. *The Pan African Medical Journal*, 25, 2016.
- [8] Benjamin Aubert, Carlos Vazquez, Thierry Cresson, Stefan Parent, and Jacques A de Guise. Toward automated 3d spine reconstruction from biplanar radiographs using cnn for statistical spine model fitting. *IEEE transactions on medical imaging*, 38(12):2796–2806, 2019.
- [9] Tamás Illés and Szabolcs Somoskeöy. The eos™ imaging system and its uses in daily orthopaedic practice. *International orthopaedics*, 36:1325–1331, 2012.
- [10] Alex Krizhevsky, Ilya Sutskever, and Geoffrey E Hinton. Imagenet classification with deep convolutional neural networks. *Advances in neural information processing systems*, 25, 2012.
- [11] Kaiming He, Xiangyu Zhang, Shaoqing Ren, and Jian Sun. Deep residual learning for image recognition. In *Proceedings of the IEEE conference on computer vision and pattern recognition*, pages 770–778, 2016.
- [12] Ashish Vaswani, Noam Shazeer, Niki Parmar, Jakob Uszkoreit, Llion Jones, Aidan N Gomez, Łukasz Kaiser, and Illia Polosukhin. Attention is all you need. *Advances in neural information processing systems*, 30, 2017.
- [13] P Maken and A Gupta. 2d-to-3d: A review for computational 3d image reconstruction from x-ray images. DOI: <https://doi.org/10.1007/s11831-022-09790-z>, pages 85–114, 2023.
- [14] D Mitton, C Landry, S Veron, Wata Skalli, F Lavaste, and Jacques A De Guise. 3d reconstruction method from biplanar radiography using non-stereocorresponding points and elastic deformable meshes. *Medical and Biological Engineering and Computing*, 38:133–139, 2000.
- [15] A Mitulescu, Wata Skalli, D Mitton, and J De Guise. Three-dimensional surface rendering reconstruction of scoliotic vertebrae using a non stereocorresponding points technique. *European spine journal*, 11:344–352, 2002.
- [16] Said Benameur, Max Mignotte, Stefan Parent, Hubert Labelle, Wafa Skalli, and Jacques de Guise. 3d/2d registration and segmentation of scoliotic vertebrae using statistical models. *Computerized Medical Imaging and Graphics*, 27(5):321–337, 2003.
- [17] Jonathan Boisvert and Daniel C. Moura. Interactive 3d reconstruction of the spine from radiographs using a statistical shape model and second-order cone programming. In *2011 Annual International Conference of the IEEE Engineering in Medicine and Biology Society*, pages 5726–5729, 2011. doi: 10.1109/IEMBS.2011.6091386.
- [18] Tristan Whitmarsh, Ludovic Humbert, Luis M Del Río Barquero, Silvana Di Gregorio, and Alejandro F Frangi. 3d reconstruction of the lumbar vertebrae from anteroposterior and lateral dual-energy x-ray absorptiometry. *Medical image analysis*, 17(4):475–487, 2013.
- [19] Vikas Karade and Bhallamudi Ravi. 3d femur model reconstruction from biplane x-ray images: a novel method based on laplacian surface deformation. *International journal of computer assisted radiology and surgery*, 10:473–485, 2015.
- [20] Emran Mohammad Abu Anas, Abtin Rasoulia, Alexander Seitel, Kathryn Darras, David Wilson, Paul St John, David Pichora, Parvin Mousavi, Robert Rohling, and Purang Abolmaesumi. Automatic segmentation of wrist bones in ct using a statistical wrist shape + pose model. *IEEE transactions on medical imaging*, 35(8):1789–1801, 2016.
- [21] Christophe Chênes and Jérôme Schmid. Revisiting contour-driven and knowledge-based deformable models: Application to 2d-3d proximal femur reconstruction from x-ray images. In *Medical Image Computing and Computer Assisted Intervention—MICCAI 2021: 24th International Conference, Strasbourg, France, September 27–October 1, 2021, Proceedings, Part VI 24*, pages 451–460, 2021.
- [22] Weinan Song, Yuan Liang, Jiawei Yang, Kun Wang, and Lei He. Oral-3d: Reconstructing the 3d structure of oral cavity from panoramic x-ray. In *Proceedings of the AAAI conference on artificial intelligence*, volume 35, pages 566–573, 2021.
- [23] Liyue Shen, Wei Zhao, and Lei Xing. Patient-specific reconstruction of volumetric computed tomography images from a single projection view via deep learning. *Nature biomedical engineering*, 3(11):880–888, 2019.
- [24] Rongjun Ge, Yuting He, Cong Xia, Chenchu Xu, Weiya Sun, Guanyu Yang, Junru Li, Zhihua Wang, Hailing Yu, Daoqiang Zhang, et al. X-ctrnsnet: 3d

- cervical vertebra ct reconstruction and segmentation directly from 2d x-ray images. *Knowledge-Based Systems*, 236:107680, 2022.
- [25] Daeun Kyung, Kyungmin Jo, Jaegul Choo, Joonseok Lee, and Edward Choi. Perspective projection-based 3d ct reconstruction from biplanar x-rays. In *ICASSP 2023-2023 IEEE International Conference on Acoustics, Speech and Signal Processing (ICASSP)*, pages 1–5, 2023.
- [26] Yoni Kasten, Daniel Doktovsky, and Ilya Kovler. End-to-end convolutional neural network for 3d reconstruction of knee bones from bi-planar x-ray images. In *Machine Learning for Medical Image Reconstruction: Third International Workshop, MLMIR 2020, Held in Conjunction with MICCAI 2020, Lima, Peru, October 8, 2020, Proceedings 3*, pages 123–133, 2020.
- [27] Ryoya Shiode, Mototaka Kabashima, Yuta Hiasa, Kunihiko Oka, Tsuyoshi Murase, Yoshinobu Sato, and Yoshito Otake. 2d–3d reconstruction of distal forearm bone from actual x-ray images of the wrist using convolutional neural networks. *Scientific Reports*, 11(1):15249, 2021.
- [28] Diogo F Almeida, Patricio Astudillo, and Dirk Vandermeulen. Three-dimensional image volumes from two-dimensional digitally reconstructed radiographs: A deep learning approach in lower limb ct scans. *Medical Physics*, 48(5):2448–2457, 2021.
- [29] Amirhossein Bayat, Anjany Sekuboyina, Johannes C Paetzold, Christian Payer, Darko Stern, Martin Urschler, Jan S Kirschke, and Bjoern H Menze. Inferring the 3d standing spine posture from 2d radiographs. In *Medical Image Computing and Computer Assisted Intervention–MICCAI 2020: 23rd International Conference, Lima, Peru, October 4–8, 2020, Proceedings, Part VI 23*, pages 775–784, 2020.
- [30] Megumi Nakao, Fei Tong, Mitsuhiro Nakamura, and Tetsuya Matsuda. Image-to-graph convolutional network for deformable shape reconstruction from a single projection image. In *Medical Image Computing and Computer Assisted Intervention–MICCAI 2021: 24th International Conference, Strasbourg, France, September 27–October 1, 2021, Proceedings, Part IV 24*, pages 259–268, 2021.
- [31] Zheyue Chen, Lijun Guo, Rong Zhang, Zhongding Fang, Xiuchao He, and Jianhua Wang. Bx2s-net: Learning to reconstruct 3d spinal structures from biplanar x-ray images. *Computers in Biology and Medicine*, 154:106615, 2023.
- [32] Han Wu, Jiadong Zhang, Yu Fang, Zhentao Liu, Nizhuan Wang, Zhiming Cui, and Dinggang Shen. Multi-view vertebra localization and identification from ct images. In *International Conference on Medical Image Computing and Computer-Assisted Intervention*, pages 136–145. Springer, 2023.
- [33] Ze Liu, Yutong Lin, Yue Cao, Han Hu, Yixuan Wei, Zheng Zhang, Stephen Lin, and Baining Guo. Swin transformer: Hierarchical vision transformer using shifted windows. In *Proceedings of the IEEE/CVF international conference on computer vision*, pages 10012–10022, 2021.
- [34] Olaf Ronneberger, Philipp Fischer, and Thomas Brox. U-net: Convolutional networks for biomedical image segmentation. In *Medical image computing and computer-assisted intervention–MICCAI 2015: 18th international conference, Munich, Germany, October 5–9, 2015, proceedings, part III 18*, pages 234–241, 2015.
- [35] Ali Hatamizadeh, Vishwesh Nath, Yucheng Tang, Dong Yang, Holger R Roth, and Daguang Xu. Swin unetr: Swin transformers for semantic segmentation of brain tumors in mri images. In *International MICCAI Brainlesion Workshop*, pages 272–284, 2021.
- [36] Yiqing Wang, Zihan Li, Jieru Mei, Zihao Wei, Li Liu, Chen Wang, Shengtian Sang, Alan L Yuille, Cihang Xie, and Yuyin Zhou. Swinmm: masked multi-view with swin transformers for 3d medical image segmentation. In *International Conference on Medical Image Computing and Computer-Assisted Intervention*, pages 486–496, 2023.
- [37] Yucheng Tang, Dong Yang, Wenqi Li, Holger R Roth, Bennett Landman, Daguang Xu, Vishwesh Nath, and Ali Hatamizadeh. Self-supervised pre-training of swin transformers for 3d medical image analysis. In *Proceedings of the IEEE/CVF conference on computer vision and pattern recognition*, pages 20730–20740, 2022.
- [38] Fausto Milletari, Nassir Navab, and Seyed-Ahmad Ahmadi. V-net: Fully convolutional neural networks for volumetric medical image segmentation. In *2016 fourth international conference on 3D vision (3DV)*, pages 565–571. Ieee, 2016.
- [39] Claude Elwood Shannon. A mathematical theory of communication. *The Bell system technical journal*, 27(3):379–423, 1948.
- [40] Ying Zhang, Tao Xiang, Timothy M Hospedales, and Huchuan Lu. Deep mutual learning. In *Proceedings of*

- the IEEE conference on computer vision and pattern recognition*, pages 4320–4328, 2018.
- [41] Natasa Milickovic, Dimos Baltas, S Giannouli, M Lahanas, and N Zamboglou. Ct imaging based digitally reconstructed radiographs and their application in brachytherapy. *Physics in Medicine & Biology*, 45(10):2787, 2000.
- [42] Jakob Wasserthal, Hanns-Christian Breit, Manfred T Meyer, Maurice Pradella, Daniel Hinck, Alexander W Sauter, Tobias Heye, Daniel T Boll, Joshy Cyriac, Shan Yang, et al. Totalsegmentator: Robust segmentation of 104 anatomic structures in ct images. *Radiology: Artificial Intelligence*, 5(5), 2023.
- [43] Yang Deng, Ce Wang, Yuan Hui, Qian Li, Jun Li, Shiwei Luo, Mengke Sun, Quan Quan, Shuxin Yang, You Hao, et al. Ctspine1k: A large-scale dataset for spinal vertebrae segmentation in computed tomography. *arXiv preprint arXiv:2105.14711*, 2021.
- [44] Anjany Sekuboyina, Malek E Husseini, Amirhossein Bayat, Maximilian Löffler, Hans Liebl, Hongwei Li, Giles Tetteh, Jan Kukačka, Christian Payer, Darko Štern, et al. Verse: a vertebrae labelling and segmentation benchmark for multi-detector ct images. *Medical image analysis*, 73:102166, 2021.
- [45] Liang Jin, Shixuan Gu, Donglai Wei, Jason Ken Adhinarta, Kaiming Kuang, Yongjie Jessica Zhang, Hanspeter Pfister, Bingbing Ni, Jiancheng Yang, and Ming Li. Ribseg v2: A large-scale benchmark for rib labeling and anatomical centerline extraction. *IEEE Transactions on Medical Imaging*, 2023.
- [46] Florian Kofler, Ivan Ezhov, Fabian Isensee, Fabian Balsiger, Christoph Berger, Maximilian Koerner, Beatrice Demiray, Julia Rakerseder, Johannes Paetzold, Hongwei Li, et al. Are we using appropriate segmentation metrics? identifying correlates of human expert perception for cnn training beyond rolling the dice coefficient. *arXiv preprint arXiv:2103.06205*, 2021.
- [47] Pietro Cerveri, Mario Marchente, Ward Bartels, Kristoff Corten, Jean-Pierre Simon, and Alfonso Manzotti. Automated method for computing the morphological and clinical parameters of the proximal femur using heuristic modeling techniques. *Annals of Biomedical Engineering*, 38:1752–1766, 2010.
- [48] Maximilian CM Fischer, Felix Krooß, Juliana Habor, and Klaus Radermacher. A robust method for automatic identification of landmarks on surface models of the pelvis. *Scientific Reports*, 9(1):13322, 2019.
- [49] Luca Di Angelo and Paolo Di Stefano. A new method for the automatic identification of the dimensional features of vertebrae. *Computer methods and programs in biomedicine*, 121(1):36–48, 2015.
- [50] Ilya Loshchilov and Frank Hutter. Decoupled weight decay regularization. In *International Conference on Learning Representations*, 2018.
- [51] Rohit Girdhar, David F Fouhey, Mikel Rodriguez, and Abhinav Gupta. Learning a predictable and generative vector representation for objects. In *Computer Vision—ECCV 2016: 14th European Conference, Amsterdam, the Netherlands, October 11–14, 2016, Proceedings, Part VI 14*, pages 484–499. Springer, 2016.
- [52] Chih-Chia Chen and Yu-Hua Fang. Using bi-planar x-ray images to reconstruct the spine structure by the convolution neural network. In *Future Trends in Biomedical and Health Informatics and Cybersecurity in Medical Devices: Proceedings of the International Conference on Biomedical and Health Informatics, ICBHI 2019, 17–20 April 2019, Taipei, Taiwan*, pages 80–85. Springer, 2020.
- [53] Ali Hatamizadeh, Yucheng Tang, Vishwesh Nath, Dong Yang, Andriy Myronenko, Bennett Landman, Holger R Roth, and Daguang Xu. Unetr: Transformers for 3d medical image segmentation. In *Proceedings of the IEEE/CVF winter conference on applications of computer vision*, pages 574–584, 2022.
- [54] Ozan Oktay, Jo Schlemper, Loic Le Folgoc, Matthew Lee, Mattias Heinrich, Kazunari Misawa, Kensaku Mori, Steven McDonagh, Nils Y Hammerla, Bernhard Kainz, et al. Attention u-net: Learning where to look for the pancreas. *arXiv preprint arXiv:1804.03999*, 2018.